Chemistry Europe
European Chemical Societies Publishing

WILEY VCH

Excellence in Chemistry Research

Announcing our new flagship journal

- Gold Open Access
- Publishing charges waived
- Preprints welcome
- Edited by active scientists

Meet the Editors of *ChemistryEurope*

Luisa De Cola
Università degli Studi di Milano Statale, Italy

Ive Hermans
University of Wisconsin-Madison, USA

Ken Tanaka
Tokyo Institute of Technology, Japan

Chemistry–A European Journal
Research Article
doi.org/10.1002/chem.202300930
Chemistry Europe
European Chemical Societies Publishing
www.chemeurj.org

Stimuli Responsive Features of Organic RTP Materials: An Intriguing Carbazole-Cyclic Triimidazole Derivative

Daniele Malpicci,[a, b] Alessandra Forni,*[b, c] Chiara Botta,[d] Clelia Giannini,[a] Elena Lucenti,[b, c] Daniele Marinotto,[b, c] Daniele Maver,[a, b] Lucia Carlucci,*[a] and Elena Cariati*[a, b, c]

Abstract: Stimuli responsive luminescent materials possessing room temperature phosphorescence (RTP) are extremely desirable for various applications. The here investigated derivative of cyclic triimidazole (**TT**) functionalized with carbazole (**Cz**), namely **TT-Ph-Cz**, belongs to this class. **TT-Ph-Cz** possesses high conformational freedom resulting in rigidochromic and multi-stimuli responsive emissive behavior. It has been isolated as MeOH-solvated and de-solvated forms characterized by distinctive emissive features. In particular, the solvated form, in which hydrogen bonds with MeOH inhibit competitive non-radiative deactivation channels, possesses a higher quantum yield associated with a strong phosphorescence contribution which is preserved in DMSO/water solutions.

Introduction

Single component organic materials characterized by rich emissive behavior including room temperature long lived features are receiving ever growing attention from the scientific community. Among the benefits they offer with respect to the widely used metal containing phosphorescent counterparts, biocompatibility and low cost represent a strong point for application in several fields such as bioimaging,[1–4] anti-counterfeiting,[5–7] catalysis[8] and displays.[9] Many strategies spanning from π-π stacking interactions[10–13] to supramolecular approaches,[14–19] crystallization[20,21] and cocrystallization,[22] halogen bonding[23,24] and doping in a polymer matrix[25] have been developed to realize materials displaying organic room temperature phosphorescence (RTP). Concomitantly, stimulus-responsive luminescent materials with adjustable and distinctive emission colors have been the subject of intense research on account of their promising applications for high-level information storage, security protection and multicolor cellular imaging.[26–31]

In this context, we have reported on a family of compounds having triimidazo[1,2-*a*:1′,2′-*c*:1″,2″-*e*][1,3,5]triazine, **TT**,[12] as core. **TT** is characterized by aggregation-induced emissive behaviour, displaying, in particular, ultralong phosphorescence (up to 1 s) under ambient conditions associated with the presence of strong π-π stacking interactions in the crystalline structure.[10] The presence of one or multiple heavy atoms or chromophoric fragments on the **TT** scaffold greatly modifies both its molecular and solid state photophysical behaviour resulting in a complex excitation dependent photoluminescence with emissions comprising dual fluorescence, molecular phosphorescence and supramolecular RTP.[13,32–39]

Carbazole, **Cz**, and its derivatives represent one of the most investigated RTP family.[17,40–44] In 2021 Liu and co-workers reported that commercially available **Cz** is mixed with traces of its isomer (1*H*-benzo[*f*]indole), which is involved in the origination of carbazoles RTUP.[45,46] This important discovery has stimulated further research on pure or doped carbazole RTP derivatives.[47–51]

Herein, we describe the synthesis, structures and photoluminescent behavior of 3-(4-(9*H*-carbazol-9-yl)phenyl)triimidazo[1,2-*a*:1′,2′-*c*:1″,2″-*e*][1,3,5]triazine, **TT-Ph-Cz** (Scheme 1). **TT-Ph-Cz** crystallizes in three different forms, one of them (**TT-Ph-CzM**) containing co-crystallized methanol and able to convert by thermal treatment to two different solvent-free structures (**TT-Ph-CzT** and **TT-Ph-CzO**) according to the temperature. The crystalline form obtained by moderate heating (**TT-Ph-CzT**), containing large voids, can interconvert to the solvated one by MeOH vapor exposure. On the other side, the more compact solvent free phase (**TT-Ph-CzO**) is not prone to uptake MeOH vapors. Photophysical characterization in solutions,

[a] *Dr. D. Malpicci, Dr. C. Giannini, Dr. D. Maver, Prof. L. Carlucci, Prof. E. Cariati*
Department of Chemistry
Università degli Studi di Milano
via Golgi 19, 20133 Milano (Italy)
E-mail: lucia.carlucci@unimi.it
elena.cariati@unimi.it

[b] *Dr. D. Malpicci, Dr. A. Forni, Dr. E. Lucenti, Dr. D. Marinotto, Dr. D. Maver, Prof. E. Cariati*
Institute of Chemical Sciences and Technologies "Giulio Natta" (SCITEC) of CNR
via Golgi 19, 20133 Milano (Italy)
E-mail: alessandra.forni@scitec.cnr.it

[c] *Dr. A. Forni, Dr. E. Lucenti, Dr. D. Marinotto, Prof. E. Cariati*
INSTM Research Unit of Milano
via Golgi 19, 20133 Milano (Italy)

[d] *Dr. C. Botta*
Institute of Chemical Sciences and Technologies "Giulio Natta" (SCITEC) of CNR
via Corti 12, 20133 Milano (Italy)

Supporting information for this article is available on the WWW under https://doi.org/10.1002/chem.202300930

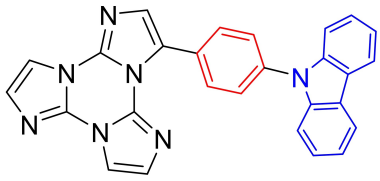

Scheme 1. Chemical structure of **TT-Ph-Cz**.

blended PMMA films and crystals of the three different phases is reported. Through X-ray diffraction (XRD) analysis, DFT/TDDFT calculations and spectroscopic investigations, the origin of the multi stimuli-responsive dual fluorescence and dual phosphorescence of **TT-Ph-Cz**, is interpreted. Moreover, nanoaggregates of **TT-Ph-Cz** prepared from solvent/non-solvent mixture are characterized by RTP features opening to their exploitation in the bioimaging field. Importantly, since multiple emissions are often to be associated with impurities, many batches of the compound were photophysically and chemically analyzed (^{1}H NMR and HPLC) to assess reproducible behaviors and exclude impurities concerns. Additionally, the same results have been observed for **TT-Ph-Cz** samples obtained either from commercial or laboratory-prepared 9*H*-carbazole-9-(4-phenyl) boronic acid pinacol ester allowing to further assign the observed emissive features to **TT-Ph-Cz** itself and not to trace amounts of different compounds.

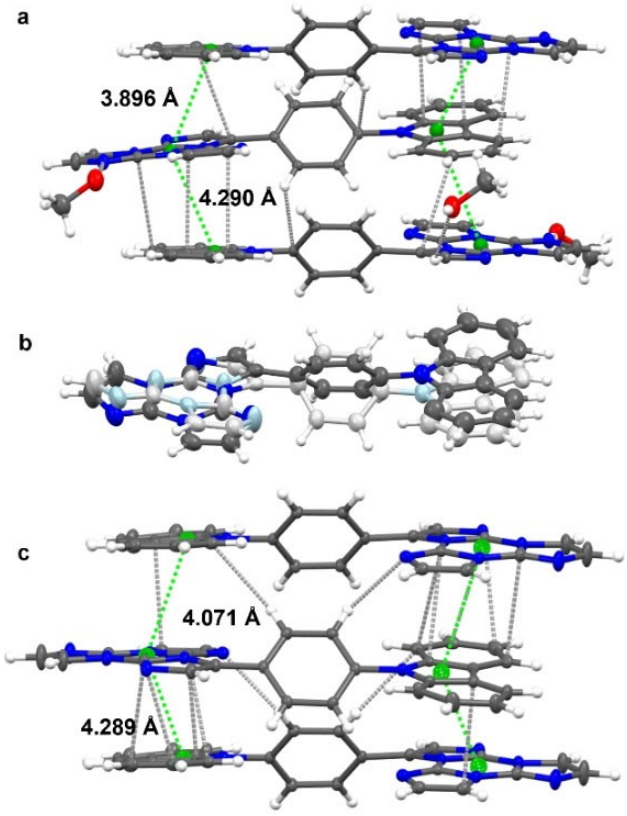

Figure 1. Crystal structures of a) **TT-Ph-CzM**, b) **TT-Ph-CzT**, showing the two disordered forms by different color gradation, and c) **TT-Ph-CzO**. In a) and c), the shorter distances between triazinic and pyrrolic geometrical centroids (green spheres) and intermolecular contacts shorter than the sum of vdW radii (light grey dashed lines) are reported. Ellipsoids at 30% probability.

Results and Discussion

Synthesis and Crystal Structure

TT-Ph-Cz has been synthetized by Suzuki coupling between the monobrominated derivative of **TT**, namely 3-bromotriimidazo[1,2-*a*:1′,2′-*c*:1″,2″-*e*][1,3,5]triazine, and either commercial or laboratory synthetized 9*H*-carbazole-9-(4-phenyl) boronic acid pinacol ester (see Supporting Information for details). It crystallizes from DCM/MeOH solutions as colorless needles including, in its asymmetric unit, one MeOH molecule in 1:1 ratio with the chromophore (**TT-Ph-CzM**, monoclinic C2/c) (Figure 1a, S4 and Table S1). In **TT-Ph-CzM**, TT and Cz are almost coplanar (the dihedral angle θ between their least-squares (l.s.) planes measuring 9.5°), while the central Ph ring is rotated from the TT and Cz least squares planes by $\theta_1 = 52.0°$ and $\theta_2 = 43.0°$, respectively. The crystal structure is governed by the formation of columnar π···π aggregates along *b*, where TT and Cz overlap with distances between triazinic and pyrrolic geometrical centroids (Cg) alternately equal to 3.896 and 4.290 Å and several short (i.e., < 3.4 Å) C···C contacts. Adjacent Ph rings along the columns lie almost perpendicular to each other ($\theta = 81.4°$) so as to form weak intermolecular C–H···π hydrogen bonds (HBs) with *r*(H···A) = 2.70 and 2.83 Å. The columns are laterally connected through relatively strong C–H···N HBs between centrosymmetry-related TT units and weaker HBs (Table S2), forming slightly corrugated planes along *ac*. The cocrystallized MeOH is rather strongly connected to TT with oxygen acting as both HB donor, with *r*(H···N) = 1.99 Å, and acceptor, *r*(H···O) = 2.57 Å, along the *c* direction (Table S2). Upon standing in air for some weeks, or by heating at 393 K, crystals of **TT-Ph-CzM** loose the cocrystallized MeOH while retaining the crystallinity at some degree, as demonstrated by both powder (see below) and single crystal XRD. **TT-Ph-CzM** is in fact proven to undergo, upon loss of MeOH, a single-crystal-to-single-crystal (SC-to-SC) transition allowing to identify the new phase as a triclinic P-1 one, **TT-Ph-CzT** (Figure 1b, Table S1). Due to the arisen voids and the increased molecular flexibility, the newly formed structure is affected by large disorder with the three composing moieties statistically occupying two equiprobable positions, A and B. The distance between corresponding A and B atoms increases in the order TT < Cz < Ph, providing a direct visualisation of the possible mobility of **TT-Ph-Cz** within the crystal. In particular, Ph statistically assumes two possible orientations almost perpendicular to each other, so as to generate an ···A···B···A···B··· arrangement similar to that found in **TT-Ph-CzM** though characterized by slightly stronger intermolecular C–H···π HBs (*r*(H···A) = 2.58 and 2.91 Å). A minor crystal packing rearrangement is observed going from **TT-Ph-CzM** to **TT-Ph-CzT**. Also in the latter, in fact, the molecules form columnar aggregates along *a*, where TT and Cz overlap with

shorter Cg···Cg distances alternately equal to 3.53 and 4.33 Å. Further heating at 443 K reveals, by X-ray powder diffraction, XRPD, analysis (see below), the formation of a new, voids free, crystalline phase. While single crystals suitable for XRD studies of this phase cannot be successfully obtained by heating single crystals of **TT-Ph-CzM** solvated phase, recrystallization from DCM (rather than DCM/MeOH) solutions allows to assign the new crystal structure to the orthorhombic Pbca space group, **TT-Ph-CzO** (Figure 1c, Table S1). Both the molecular conformation and the π-stack motif are essentially unvaried with respect to **TT-Ph-CzM** (θ, θ_1 and θ_2 measure 10.4°, 54.8° and 45.0°, respectively; Cg···Cg distances are alternately equal to 4.071 and 4.289 Å). However, in **TT-Ph-CzO** even stronger intermolecular C–H···π HBs between adjacent phenyl rings are found (r(H···A) = 2.50 and 2.75 Å) compared to **TT-Ph-CzM** and **TT-Ph-CzT**. Interestingly, while variations <1% are observed along the shortest and the longest crystallographic axes, a shrinking by 8% is found along the intermediate axis, i.e., along the direction where, in **TT-Ph-CzM**, the HB motif with MeOH develops (Table S1 and Figure S5).

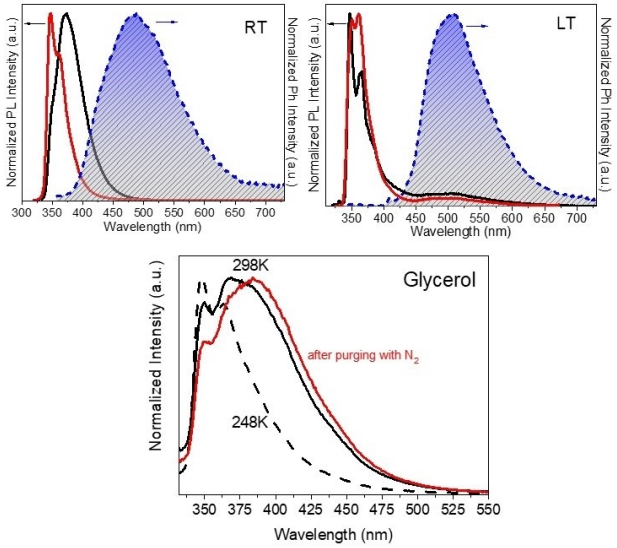

Figure 2. TT-Ph-Cz normalized emission spectra (λ_{exc} = 300 nm). Top: PL of DCM solutions (2×10^{-6} M, black lines) at 298 K (left) and 77 K (right) in air. PL of PMMA films (0.5 wt%, at 298 K, left, and 90 K, right) in vacuum (red) and delayed spectra (blue dashed, delay 0.2 ms, window 0.5 ms). Bottom: PL in glycerol (2×10^{-6} M) at 248 K (black dashed line) and 298 K (black continuous line); after N_2 purging for 10 min at 298 K (red continuous line).

Table 1. Photophysical parameters of **TT-Ph-CzM**, **TT-Ph-CzT** and **TT-Ph-CzO**.

TT-Ph-Cz		298 K		77 K	
	Φ %	λ_{em}	τ_{av}[a]	λ_{em}	τ_{av}[a]
DCM	63	350	2.86 ns	353	5.60 ns
		370		512	935 ms
PMMA	60	347	7.70 ns	350	8.79 ns[b]
		360			
		490	246.8 ms	508	601.0 ms[b]
TT-Ph-CzM	43	375	2.16 ns	373	3.45 ns
		408		388	
		425	20.72 ms		
		540	60.94 ms	523	684.47 ms
TT-Ph-CzT	22	374	3.41 ns		
		394			
		432	3.03 ms		
		525	10.61 ms		
TT-Ph-CzO	23	373	3.49 ns		
		416	15.04 ms		
		550	62.16 ms		

[a] Calculated by $\tau_{av} = \frac{\sum_{n=1}^{m} \alpha_n \tau_n^2}{\sum_{n=1}^{m} \alpha_n \tau_n}$. [b] At 90 K.

Photophysical investigation in solution and PMMA films

TT-Ph-Cz shows at 298 K in DCM (2×10^{-6} M, Figure 2) solutions four absorption maxima at 236, 293, 310 and 340 nm (Figure S6) and a broad fluorescence at 370 nm with a weak shoulder at 350 nm (Φ = 63%, τ = 2.86 ns, Table 1, Figure S7). Both absorption and emission maxima do not show significant solvatochromic shifts in solvents of different dielectric constant (Figure S11) in agreement with the low polarity of both ground and first singlet excited state (computed dipole moments equal to 1.25 and 3.24 D, respectively, the latter computed at the Franck-Condon geometry).

At 77 K in DCM, a narrowing of the band, with maximum shifted to 353 nm (τ = 5.60 ns, Figure S9), is observed together with the appearance of a broad phosphorescence centred at 512 nm (τ = 935 ms, Figure S10). This latter contribution seems to be reasonably assigned (based on its similarity to what observed for other members of the **TT** family and **TT-Ph-Cz** in crystals and PMMA blended films, see later) to aggregated species whose presence in frozen DCM cannot be excluded despite the use of diluted solutions.[33,35] To better clarify the molecular behaviour of **TT-Ph-Cz**, PMMA blended films (**TT-Ph-Cz** 0.5 wt%) have been prepared and characterized in vacuum at both 298 (Φ = 60.2%) and 90 K (Figure 2). The films display at both temperatures one narrow fluorescence with vibronic replicas at 347 and 360 nm (τ = 7.70 and 8.79 ns, at 298 and 90 K, respectively; Figures S14 and S15), together with a broad structureless phosphorescence. This long-lived component is already visible in photoluminescent (PL) spectra at 90 K but recognizable at both temperatures through delayed measurements (490 nm, τ = 246 ms at 298 K and 508 nm, τ = 601 ms at 90 K, Figures S16 and S17). Again, the most probable origin of this emission seems to be associated to aggregated species which can be present and observed in PMMA matrix even at very low chromophore loading. Importantly, in this regard, both molecular phosphorescence (at about 415 nm) and supramolecular one (at about 510 nm), have been detected for the related **TT-(C)-Cz** derivative (where **TT** and **Cz** are directly connected through a C–C covalent bond) in PMMA films (0.5 wt%) at 298 and 90 K.[39]

To further support this hypothesis, PMMA blended films with lower (0.1 wt%) and higher (5 wt%) loadings have been prepared. The films are characterized by the same fluorescence when excited at 300 nm. However, at 370 nm excitation, the additional broad low energy emission is clearly recognizable, even at 298 K, only in the PL spectrum of the film with the

highest (5 wt%) loading (Figure S18). Similarly, in delayed spectra collected at 298 K, the intensity of such long lived component increases with chromophore loadings supporting its aggregated origin (Figure S19).

The comparison of the fluorescence spectra of Figure 2 highlights that the emission of the compound in solution at RT is quite different from that observed in PMMA and solution at 77 K, suggesting rigidification effects on the emissive features of **TT-Ph-Cz**. Therefore, more experiments were performed to deepen this aspect. In particular, emissions from highly viscous solvent were monitored. **TT-Ph-Cz** in glycerol (2×10^{-6} M, Figure 2) at 298 K clearly shows two emissive components resulting in a broad band centred at 380 nm ($\tau=4.13$ ns, Figure S22) and a narrow peak at 350 nm ($\tau=3.09$ ns, Figure S21). The relative intensity of the two components varies with oxygen content. In particular, the 380 nm band is intensified when purging the solution with nitrogen for 10 min. By keeping the glycerol solution in a freezer at 248 K for 15 min to increase its viscosity, the 380 nm component appears totally quenched and gradually restored by returning to 298 K (Figure S23).

These results can be rationalized through the presence of a Frank Condon (FC) emitting state (S_1^{FC}) and a relaxed one (S_1^{rel}): when molecular conformation is somehow locked either in frozen solution or in PMMA, the FC state is the main responsible of the emission, resulting in the high energy fluorescence at 350 nm (HEF); on the other side, in fluid solution at RT, both singlet states can be populated producing a broader emission in which a low energy contribution at about 370 nm (LEF) can be recognized as clearly identified by increasing the viscosity of the medium (as represented in the simplified Jablonski diagrams of Figure 3).

Theoretical calculations

The presence of different RT thermally equilibrated minima in S_1 was confirmed by theoretical calculations on **TT-Ph-Cz** (Figures S62–S64 and Table S3). The electronic levels, all corresponding to (π,π^*) transitions and, at low energy, mainly localized on Cz (in particular S_1 and T_1), denote partial molecular conjugation. Relaxed potential energy surface (PES) scans fixing the relative orientation of either TT–Ph or Cz–Ph and scanning that of Cz–Ph or TT–Ph, respectively, reveal the presence of two minima in S_1 (Figure 4 for the former calculations; quite similar results are obtained for the latter). One corresponds to the FC state and its free optimization leads to a locally relaxed X-ray molecular geometry (S_1^{FC}). The other minimum, separated from the former by a ~1 kcal/mol barrier, corresponds to a geometry where the TT and Ph (or Cz and Ph) are almost coplanar. Free optimization of this geometry leads to the absolute minimum (S_1^{rel}) characterized by slightly increased twisting of TT and Cz but greater coplanarity between TT and Ph ($\theta=20.6$, $\theta_1=24.2$, $\theta_2=40.4°$), allowing an effective conjugation and therefore explaining the corresponding red-shift and intensification with respect to the locally excited minimum. Such S_1^{rel} conformation lies very close to a triplet state (T_4, 0.02 eV below S_1^{rel}, Figure S63) whose fingerprint cannot be detected in solution even after three freeze-pump-thaw cycles due to the presence of more efficacious competitive non-radiative deactivation channels (such as molecular rotations). However, the involvement of the triplet state in the photophysics of molecular **TT-Ph-Cz** can be guessed by the effect of N_2 purging in glycerol (Figure 2).

Solvent/non-solvent experiments

Emission in solvent/non-solvent (DMSO/water) mixtures was explored (Figure 5). Addition of increasing volumes of water to DMSO solutions (keeping the concentration of **TT-Ph-Cz** equal to 2×10^{-6} M) results in a red shift of the emission maximum of the broad band (from 370 nm in DMSO to 430 nm in DMSO/water 20/80%). More precisely, while the fluorescence contribu-

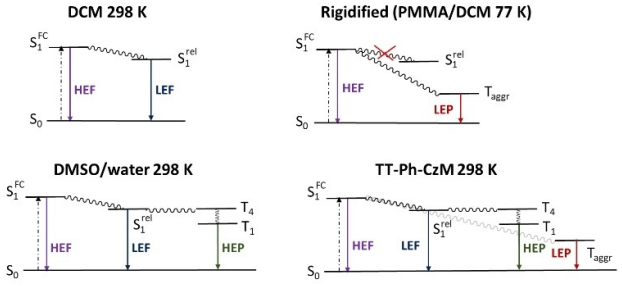

Figure 3. Simplified Jablonski diagrams for DCM solution at 298 K, PMMA film and glassy DCM solution, aggregates in solvent-non solvent mixtures and crystals of **TT-Ph-CzM** at 298 K.

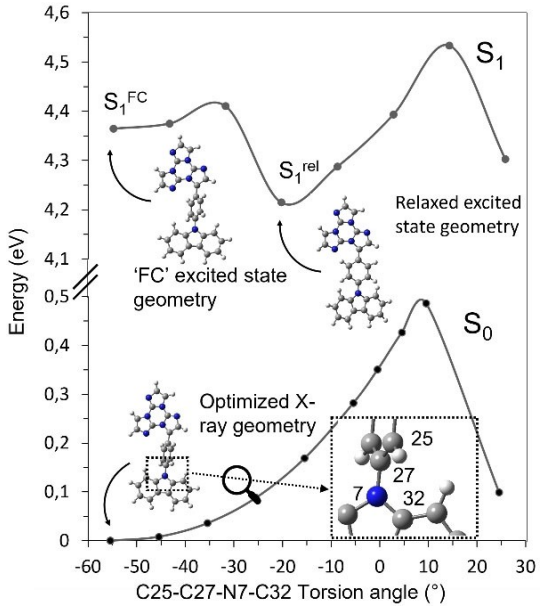

Figure 4. Scan of the relaxed potential energy surface of the S_0 and S_1 states of **TT-Ph-Cz** along the C25-C27-N7-C32 torsion angle at the (TD)-ωB97X/6-311++G(d,p) level of theory. Energies are relative to the S_0 state equilibrium geometry.

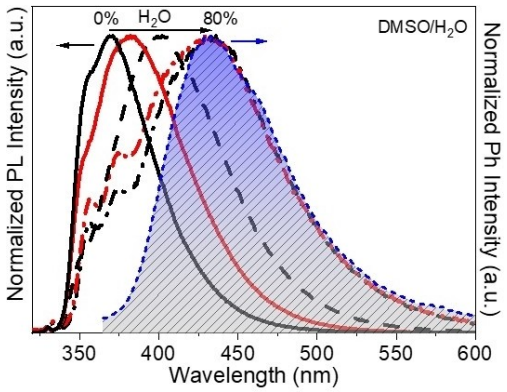

Figure 5. TT-Ph-Cz normalized emission spectra ($\lambda_{exc}=300$ nm) at 298 K in DMSO (2×10^{-6} M) with increasing H_2O volume. 0% (black continuous), 20% (red continuous), 50% (black dashed), 70% (red dashed-dotted), 80% (black dashed-dotted). Delayed spectrum (blue dashed, delay 0.2 ms window 0.5 ms) of the 80% water fraction solution.

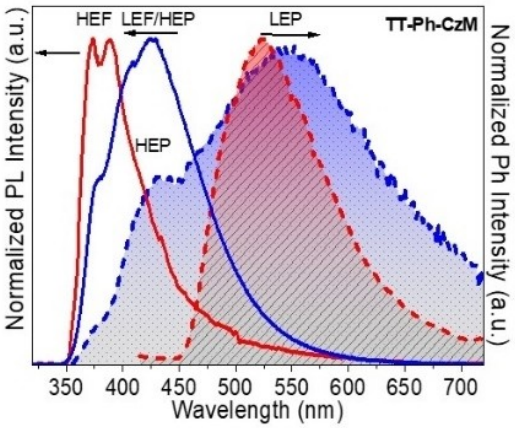

Figure 6. Normalized emission spectra ($\lambda_{exc}=300$ nm) of **TT-Ph-CzM** crystals. PL at 298 K (blue continuous) and 77 K (red continuous). Delayed spectra at 298 K (blue dashed, delay 0.2 ms, window 0.5 ms) and 77 K (red dashed, delay 1 ms, window 5 ms).

tion at high energy is still visible but highly quenched, a new long-lived component gradually emerges at lower energy in DMSO/water solutions with increasing water amounts. Such phosphorescence can be easily detected in delayed spectra of the 80% water fraction solution (Figure 5, $\tau=28.52$ ms, Figures S26 and S27).

This RT phosphorescence is probably of molecular origin (see relative Jablonski diagram reported in Figure 3) based on its closeness to the molecular S_1^{rel} and its distance from the aggregated phosphorescence observed at about 500 nm in PMMA, frozen DCM and crystals (see later). In DMSO at 298 K both S_1^{FC} and S_1^{rel} singlets can be populated resulting in a broad fluorescence as observed in DCM. It is reasonable to hypothesize that the addition of water results in the formation of poorly organized nanoaggregates where intermolecular interactions suppress competitive non-radiative deactivation channels (i.e., reduced molecular movements and protection from oxygen quenching) favouring the red shifted emission (molecular phosphorescence through ISC from S_1^{rel} to T_4 followed by IC to T_1).

Moreover, solvent/non-solvent experiments have allowed to monitor the temporal evolution of the aggregate formation as a function of chromophore concentration. In particular, while the phosphorescence at 430 nm almost instantaneously prevails on fluorescence for the 10^{-5} M solution, the relative intensity of the two components varies with time for more diluted solutions. In fact, phosphorescence becomes the predominant contribution faster for the 2×10^{-6} M than for the 1×10^{-6} M solution (see Figures S29 and S31).

Photophysical investigation on crystals

Solid state measurements (Table 1) were performed on **TT-Ph-CzM** crystals obtained from DCM/MeOH (Figure 6). When exciting at 300 nm at 298 K, a multicomponent emission comprising one broad band centred at about 425 nm ($\tau=$ 20.72 ms, Figure S36) with high energy shoulders at 375 and 408 nm ($\tau=2.16$ ns, Figure S35) (overall $\Phi=43\%$) is observed. The nature of the 425 nm contribution is better disclosed from time resolved measurements revealing the presence of a long-lived component (HEP). Moreover, an additional phosphorescence at 540 nm (LEP, $\tau=60.94$ ms, Figure S37) emerges from the delayed experiments. At 77 K, the high energy fluorescence (HEF) becomes highly predominant in the PL spectrum while a single phosphorescence at 523 nm appears in the delayed one (LEP, $\tau=684.47$ ms, Figure S40). The absence of HEP at 77 K resembles what observed in frozen DCM solution and can be analogously rationalized with the presence of two conformations in the singlet excited state. More specifically, a S_1^{FC} state and a relaxed one (S_1^{rel}), the latter not accessible at low temperature due to the locked conformation. The closeness of S_1^{rel} to a triplet state allows intersystem crossing (ISC) resulting, at room temperature, in molecular phosphorescence (HEP). The broad 425 nm emission observed at 298 K might therefore contain both the S_1^{rel} fluorescence (LEF) and HEP.

LEP, resembling that of frozen DCM solution and PMMA blended films, could be associated to the π-π stacked motif present in this structure, as already reported for other TT-derivatives and **TT** itself.[12] Importantly, both HEP and LEP can be observed being originated from different entities (molecule and aggregate). A similar result was obtained for crystals of brominated derivatives of **Ph-Cz** having two long-lived emissions ascribed to deactivation from molecular T_1 (430 nm) and aggregated structure T_n* (550–600 nm).[52]

As mentioned, three different crystal structures have been isolated for **TT-Ph-Cz**, therefore different emissive features were expected and indeed observed at 298 K for differently treated batches (Figure 7).

By exciting at 300 nm, it is observed that the relative intensity of the combined LEF/HEP contribution is decreased with respect to HEF when **TT-Ph-CzM** is kept open in air for few weeks, by thermal treatment or grinding (conditions which are

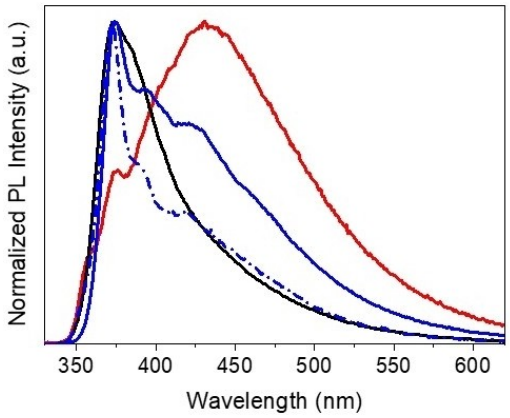

Figure 7. Normalized PL emission spectra displaying the stimuli responsiveness of the **TT-Ph-CzM** crystals high energy bands at 298 K ($\lambda_{exc} = 300$ nm): ground crystals (black), ground crystals after exposure to MeOH vapours for 30 min (red), crystals heated at 393 (blue) or 443 K (blue dashed dot) for 90 min.

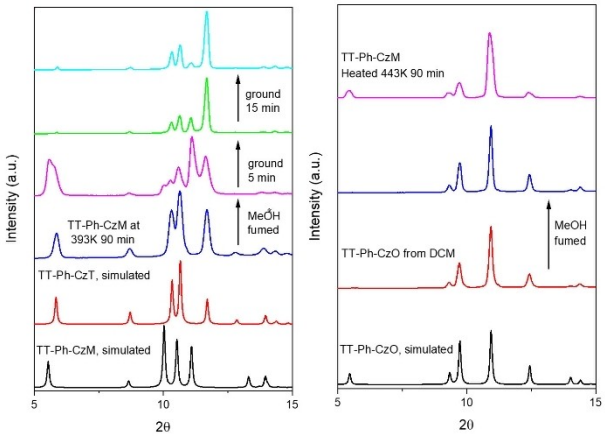

Figure 8. Simulated and experimental XRPD spectra. Left: **TT-Ph-CzM** heated at 393 K for 90 min (blue), exposed to MeOH vapors (magenta) and after successive grinding (green and cyan). Right: **TT-Ph-CzO** from DCM (red), exposed to MeOH vapors (blue) and **TT-Ph-CzM** heated at 443 K for 90 min (magenta).

all expected to favor MeOH release). Moreover, a decrease in the quantum yield is observed after external stimuli perturbations. In particular, Φ of **TT-Ph-CzM** crystals decreases to 22% and 23% after heating at 393 or 443 K for 90 min, respectively, and to 17% after grinding in a mortar. Exposure to MeOH vapors for few minutes of either the 393 K heated or mechanically treated **TT-Ph-CzM** crystals, results in restoring the original HEP/LEF and Φ. This behavior has been assessed for multiple cycles through XRPD (see later) and photophysical analysis. Importantly, the same enhancement was observed also through exposure to water vapors of **TT-Ph-CzM** after "mild" thermal treatment (Figure S56).

The origin of this stimuli-responsiveness was investigated through thermal and XRD analysis. In the heating process, MeOH molecules can be released, as confirmed by thermogravimetric analysis (TGA) of **TT-Ph-CzM** crystals with a gradual weight loss of about 6% (calculated 6.8%) from RT to 423 K and with decomposition temperature at about 573 K (Figure S47). The MeOH release is accompanied by a modification of the crystal structure as resulted from the evident changes in the XRPD patterns (Figure 8) and confirmed by single crystal XRD data on **TT-Ph-CzT** and **TT-Ph-CzO**. In particular, by release of MeOH in mild conditions (grinding, standing in air at RT or 393 K), **TT-Ph-CzT** is obtained. Such desolvated phase can restore **TT-Ph-CzM** (and its emission) by exposure to MeOH vapors (Figure 9). Heating at 443 K, results in the formation of **TT-Ph-CzO** which is not prone to be transformed into **TT-Ph-CzM** by MeOH uptake due to its more compact structure with respect to **TT-Ph-CzT** (Figure 8)

The photophysical investigation on **TT-Ph-CzT** (obtained from **TT-Ph-CzM** heated at 393 K for 90 min, Figure 10) and **TT-Ph-CzO** (crystallized from DCM solutions, Figure 11) adds further details on the mechanisms involved in the observed multiemissive behavior.

When exciting at 300 nm, the PL spectrum of **TT-Ph-CzT** displays a multicomponent emission dominated by a narrow

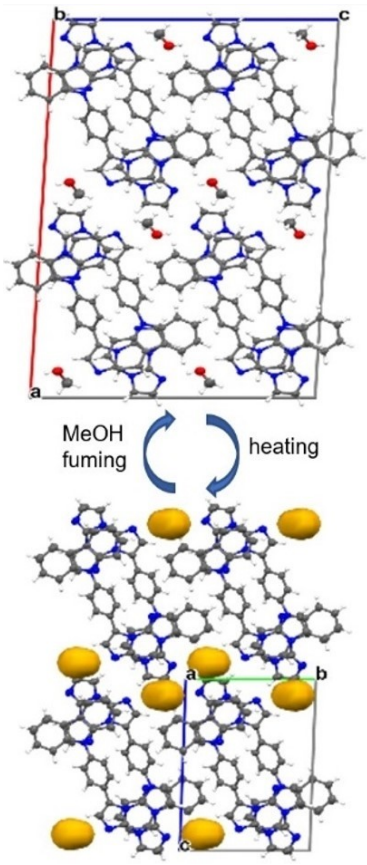

Figure 9. Packing of **TT-Ph-CzM** (top) and **TT-Ph-CzT** (bottom) with the solvent-accessible empty spaces visualized by yellow surfaces generated with a spherical probe of radius 1.2 Å. For **TT-Ph-CzT**, only one of the two equiprobable positions is shown.

peak at 374 nm (HEF, $\tau = 3.41$ ns, Figures 10 and S49). The broader LEF/HEP contribution can be selectively observed by exciting at 375 nm being otherwise overwhelmed by the

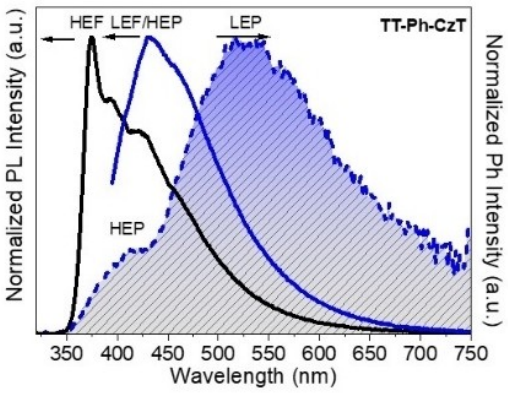

Figure 10. Normalized PL spectra (black line, $\lambda_{exc} = 300$ nm; blue line, $\lambda_{exc} = 375$ nm) and phosphorescence spectrum (blue line, $\lambda_{exc} = 300$ nm, delay 0.2 ms, window 0.5 ms) at 298 K of **TT-Ph-CzT** obtained from **TT-Ph-CzM** crystals heated at 393 K for 90 min.

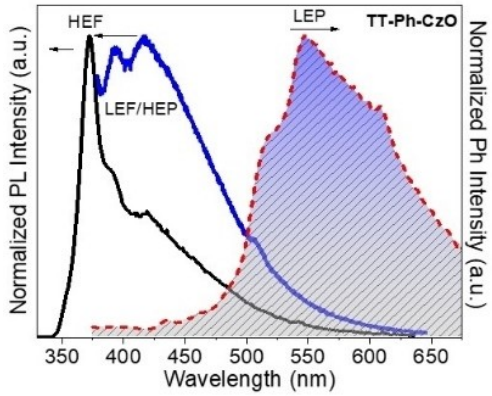

Figure 11. Normalized PL spectra (black line, $\lambda_{exc} = 300$ nm; blue line, $\lambda_{exc} = 370$ nm) and phosphorescence spectrum (red line, $\lambda_{exc} = 360$ nm, delay 1 ms, window 5 ms) of **TT-Ph-CzO** crystals at 298 K.

stronger HEF. In addition, the presence of LEP at 525 nm ($\tau =$ 10.61 ms, Figure S51) emerges from delayed experiments. The weakness of the HEP does not allow its clear identification from delayed spectra. However, the presence of a long-lived component is suggested from lifetime measurements ($\tau =$ 3.03 ms, Figure S50).

When exciting at 300 nm, the PL spectrum of **TT-Ph-CzO** is dominated by a narrow peak at 373 nm (HEF, $\tau = 3.49$ ns, Figures 11 and S58), while a broader LEF/HEP appears only by exciting at 370 nm being otherwise overwhelmed by the stronger HEF. From delayed experiments, LEP clearly emerges at 550 nm ($\tau = 62.16$ ms, Figure S60), while HEP appears only as a very weak signal at about 430 nm. In fact, HEP could not be well disentangled from LEP in the delayed spectra due to its much lower efficiency. However, a long-lived HEP component at 416 nm is clearly identified from lifetime measurements ($\tau =$ 15.04 ms, Figure S59).

A direct comparison between the high energy components observed in PL spectra of the three crystalline phases (Figure 7) nicely illustrates the role of molecular flexibility in the photophysical behaviour of the investigated compound. In **TT-Ph-CzM**, the co-crystallized MeOH, strongly connected to the TT unit through HB, from one side allows conformational freedom to the Ph–Cz fragment of the molecule (so that S_1^{rel} can be populated), on the other side contributes to rigidify the structure and to suppress non-radiative deactivation channels highly competitive with the phosphorescent emission. This results in attenuated HEF and intense HEP/LEF.[14,53,54] In **TT-Ph-CzT**, lacking MeOH but having large voids inside the crystal structure, S_1^{rel} can be easily populated but LEF/HEP is attenuated due to the increased molecular motions. Finally, in **TT-Ph-CzO**, it is hypothesized that the molecular flexibility is much reduced with respect to the other phases owing to the relatively strong C–H···π HBs interconnecting adjacent phenyl rings, preventing relaxation from S_1^{FC} to S_1^{rel} and therefore privileging HEF rather than LEF/HEP.

Conclusions

TT-Ph-Cz possesses conformational freedom resulting in rigidochromic and multistimuli responsive behaviour. In fact, its computed singlet excited state possesses two minima, a Frank Condon and a relaxed one, whose population depends on external conditions: in fluid solution, photoluminescence originates from both conformations resulting into a broad fluorescence while, in rigid matrices or at 77 K, only the FC state is sufficiently populated resulting in a narrow, high energy fluorescence. Since a triplet state is close to the relaxed excited singlet, phosphorescence can be observed when competitive deactivation channels are suppressed. This happens in the aggregates, in particular for DMSO/water nanoaggregates and crystals of the MeOH solvated form, **TT-Ph-CzM**, where HBs reduce molecular movements responsible for non-radiative dissipation of energy excess.

TT-Ph-CzM evolves, through thermal treatment, to **TT-Ph-CzT** and **TT-Ph-CzO**. The former is obtainable from "mild" desolvation of **TT-Ph-CzM** according to a SC-to-SC process and it is able to reconvert to the original phase by MeOH vapours uptake. The latter derives by "strong" thermal treatment and can be directly prepared from methanol-free solutions. According to the compact molecular organization in **TT-Ph-CzO**, this phase cannot be transformed into **TT-Ph-CzM** when exposed to MeOH vapours. All solid phases display HEP and LEP (LEP associated with π-π stacking interactions and HEP having mainly Cz character) with different relative contribution. HEP is, in fact, dominant in the methanol solvated phase supporting the key role of HBs in inhibiting competitive non-radiative deactivation channels.

Such multifaceted emissive behaviour, comprising dual fluorescence (clearly visible in glycerol) and phosphorescence, RTP from aqueous aggregates, mechanochromism and vapochromism, further confirms **TT** as a powerful building block in designing high-performance single-component luminescent materials.

Experimental Section

All synthesis-related information is provided in the Supporting Information.

Photophysical characterization

UV-Visible spectra are collected by a Shimadzu UV3600 spectrophotometer. Absolute photoluminescence quantum yields are measured using a C11347 (Hamamatsu Photonics K.K). A description of the experimental setup and measurement method can be found in the article of K. Suzuki et al.[55] For any fixed excitation wavelength, the fluorescence quantum yield Φ is given by:

$$\Phi = \frac{\mathrm{PN(Em)}}{\mathrm{PN(Abs)}} = \frac{\int \frac{\lambda}{hc}\left[I_{em}^{sample}(\lambda) - I_{em}^{reference}(\lambda)\right] d\lambda}{\int \frac{\lambda}{hc}\left[I_{ex}^{reference}(\lambda) - I_{ex}^{sample}(\lambda)\right] d\lambda}$$

where PN(Em) is the number of photons emitted from a sample and PN(Abs) is the number of photons absorbed by a sample, λ is the wavelength, h is Planck's constant, c is the velocity of light, $I_{em}^{sample}(\lambda)$ and $I_{em}^{reference}(\lambda)$ are the photoluminescence intensities with and without a sample, respectively, $I_{ex}^{sample}(\lambda)$ and $I_{ex}^{reference}(\lambda)$ are the integrated intensities of the excitation light with and without a sample, respectively. PN(Em) is calculated in the wavelength interval $[\lambda_i, \lambda_f]$, where λ_i is taken 10 nm above the excitation wavelength, while λ_f is the upper end wavelength in the emission spectrum. The error made is estimated at around 5%. Steady-state emission and excitation spectra and photoluminescence lifetimes are obtained using an FLS 980 (Edinburg Instrument Ltd, Livingston, UK) spectrofluorimeter. The steady-state measurements are recorded by a 450 W Xenon arc lamp. Photoluminescence lifetime measurements are performed using: Edinburgh Picosecond Pulsed Diode Laser EPL-375, EPLED-300, (Edinburg Instrument Ltd, Livingston, UK) and microsecond flash Xe-lamp (60 W, $0.1 \div 100$ Hz) with data acquisition devices time-correlated single-photon counting (TCSPC) and multi-channel scaling (MCS) methods, respectively. Delayed spectra are collected with a NanoLog composed by an iH320 spectrograph equipped with a PPD-850 single photon detector module with Time-Gated Separation by exciting with a pulsed Xe lamp. The spectra are corrected for the instrument response. Low temperature measurements are performed in a quartz dewar by immersion of the sample in liquid nitrogen or with a variable temperature liquid nitrogen cryostat Oxford DN1704.

Crystal structure analysis

Single-crystal X-ray diffraction data for **TT-Ph-CzM**, **TT-Ph-CzT** and **TT-Ph-CzO** were collected at room temperature on a Bruker APEX II CCD area detector diffractometer, using graphite-monochromated Mo $K\alpha$ radiation ($\lambda = 0.71073$ Å). After integration, an empirical absorption correction was made on the basis of the symmetry-equivalent reflection intensities measured.[56] The structures were solved by direct methods using SHELXS[57] and subsequent Fourier synthesis; they were refined by full-matrix least-squares on F^2 (SHELXL 2018)[58] using all reflections. Weights were assigned to individual observations according to the formula $w = 1/[\sigma^2(F_o^2) + (aP)^2 + bP]$, where $P = (F_o^2 + 2F_c^2)/3$; a and b were chosen to give a flat analysis of variance in terms of F_o^2. Anisotropic parameters were assigned to all non-hydrogen atoms. Hydrogen atoms were placed in idealized position and refined riding on their parent atom with an isotropic displacement parameter 1.2 (or 1.5) times that of the pertinent parent atom. The final difference electron density map showed no features of chemical significance, with the largest peaks lying close to the center of bonds.

Crystal data, data collection and refinement details of the structural analyses are summarized in Table S1. Deposition Numbers 2193378, 2215189 and 2215190 contain the supplementary crystallographic data for **TT-Ph-CzM**, **TT-Ph-CzT** and **TT-Ph-CzO**, respectively. These data are provided free of charge by the joint Cambridge Crystallographic Data Centre and Fachinformationszentrum Karlsruhe Access Structures service.

Computational details

DFT and TDDFT calculations on isolated 'gas-phase' molecules of **TT-Ph-Cz** were performed with Gaussian 16 program (Revision A.03)[59] using the 6–311++G(d,p) basis set. The molecular geometry has been optimized starting from the experimental structure as derived from X-ray studies. Based on previous theoretical results obtained on the parent cyclic triimidazole[12] and its pyrene-,[36,37] pyridine-[35] and cloro-, bromo- and iododerivatives,[13,32,33,38] as well as on models of Ag and Cu coordination polymers of **TT**,[60,61] the ωB97X[62] functional was used owing to its ability in correctly treating at the same time not only ground and excited states properties, but also intermolecular interactions. In fact, the PBE0 and CAM-B3LYP functionals were previously found to accurately reproduce the absorption spectrum of the isolated monomers but failed to provide stable π-π stacked dimers. On the other side, the B97D functional, while providing stable π-π dimers, was found to be instable for TDDFT calculations.

Acknowledgements

The use of instrumentation purchased through the Regione Lombardia-Fondazione Cariplo joint SmartMatLab Project is gratefully acknowledged. Andrea Previtali is acknowledged for his contribution in the early stage of this research. Mass spectrometry analyses were performed at the Mass Spectrometry facility of the Unitech COSPECT at the University of Milan (Italy).

Conflict of Interests

The authors declare no conflict of interest.

Data Availability Statement

The data that support the findings of this study are available in the supplementary material of this article.

Keywords: room temperature phosphorescence · stimuli-responsive materials · time-resolved spectroscopy

[1] Q. Dang, Y. Jiang, J. Wang, J. Wang, Q. Zhang, M. Zhang, S. Luo, Y. Xie, K. Pu, Q. Li, Z. Li, *Adv. Mater.* **2020**, *32*, 1–7.
[2] Y. Wang, H. Gao, J. Yang, M. Fang, D. Ding, B. Z. Tang, Z. Li, *Adv. Mater.* **2021**, *33*, 1–8.
[3] W. Qin, P. Zhang, H. Li, J. W. Y. Lam, Y. Cai, R. T. K. Kwok, J. Qian, W. Zheng, B. Z. Tang, *Chem. Sci.* **2018**, *9*, 2705–2710.
[4] J. Zhi, Q. Zhou, H. Shi, Z. An, W. Huang, *Chem. Asian J.* **2020**, *15*, 947–957.

[5] L. Gu, H. Wu, H. Ma, W. Ye, W. Jia, H. Wang, H. Chen, N. Zhang, D. Wang, C. Qian, Z. An, W. Huang, Y. Zhao, *Nat. Commun.* **2020**, *11*, 944.
[6] Y. Lei, W. Dai, J. Guan, S. Guo, F. Ren, Y. Zhou, J. Shi, B. Tong, Z. Cai, J. Zheng, Y. Dong, *Angew. Chem. Int. Ed.* **2020**, *59*, 16054–16060.
[7] J. Tan, Q. Li, S. Meng, Y. Li, J. Yang, Y. Ye, Z. Tang, S. Qu, X. Ren, *Adv. Mater.* **2021**, *33*, 1–7.
[8] R. Gao, D. Yan, *Chem. Commun.* **2017**, *53*, 5408–5411.
[9] S. Hirata, K. Totani, H. Kaji, M. Vacha, T. Watanabe, C. Adachi, *Adv. Opt. Mater.* **2013**, *1*, 438–442.
[10] Z. An, C. Zheng, Y. Tao, R. Chen, H. Shi, T. Chen, Z. Wang, H. Li, R. Deng, X. Liu, W. Huang, *Nat. Mater.* **2015**, *14*, 685–690.
[11] L. Gu, H. Shi, L. Bian, M. Gu, K. Ling, X. Wang, H. Ma, S. Cai, W. Ning, L. Fu, H. Wang, S. Wang, Y. Gao, W. Yao, F. Huo, Y. Tao, Z. An, X. Liu, W. Huang, *Nat. Photonics* **2019**, *13*, 406–411.
[12] E. Lucenti, A. Forni, C. Botta, L. Carlucci, C. Giannini, D. Marinotto, A. Previtali, S. Righetto, E. Cariati, *J. Phys. Chem. Lett.* **2017**, *8*, 1894–1898.
[13] E. Lucenti, A. Forni, C. Botta, L. Carlucci, C. Giannini, D. Marinotto, A. Pavanello, A. Previtali, S. Righetto, E. Cariati, *Angew. Chem. Int. Ed.* **2017**, *56*, 16302–16307.
[14] L. Bian, H. Shi, X. Wang, K. Ling, H. Ma, M. Li, Z. Cheng, C. Ma, S. Cai, Q. Wu, N. Gan, X. Xu, Z. An, W. Huang, *J. Am. Chem. Soc.* **2018**, *140*, 10734–10739.
[15] X.-K. Ma, Y. Liu, *Acc. Chem. Res.* **2021**, *54*, 3403–3414.
[16] H. Mieno, R. Kabe, N. Notsuka, M. D. Allendorf, C. Adachi, *Adv. Opt. Mater.* **2016**, *4*, 1015–1021.
[17] R. Kabe, C. Adachi, *Nature* **2017**, *550*, 384–387.
[18] D. Li, F. Lu, J. Wang, W. Hu, X. M. Cao, X. Ma, H. Tian, *J. Am. Chem. Soc.* **2018**, *140*, 1916–1923.
[19] Z. Y. Zhang, W. W. Xu, W. S. Xu, J. Niu, X. H. Sun, Y. Liu, *Angew. Chem. Int. Ed.* **2020**, *59*, 18748–18754.
[20] M. Hayduk, S. Riebe, J. Voskuhl, *Chem. Eur. J.* **2018**, *24*, 12221–12230.
[21] M. Baroncini, G. Bergamini, P. Ceroni, *Chem. Commun.* **2017**, *53*, 2081–2093.
[22] L. Sun, W. Zhu, F. Yang, B. Li, X. Ren, X. Zhang, W. Hu, *Phys. Chem. Chem. Phys.* **2018**, *20*, 6009–6023.
[23] O. Bolton, K. Lee, H.-J. Kim, K. Y. Lin, J. Kim, *Nat. Chem.* **2011**, *3*, 205–210.
[24] H. Shi, Z. An, P.-Z. Li, J. Yin, G. Xing, T. He, H. Chen, J. Wang, H. Sun, W. Huang, Y. Zhao, *Cryst. Growth Des.* **2016**, *16*, 808–813.
[25] Z. Lin, R. Kabe, N. Nishimura, K. Jinnai, C. Adachi, *Adv. Mater.* **2018**, *30*, 1803713.
[26] K. Jiang, S. Sun, L. Zhang, Y. Lu, A. Wu, C. Cai, H. Lin, *Angew. Chem. Int. Ed.* **2015**, *54*, 5360–5363.
[27] L. Pan, S. Sun, A. Zhang, K. Jiang, L. Zhang, C. Dong, Q. Huang, A. Wu, H. Lin, *Adv. Mater.* **2015**, *27*, 7782–7787.
[28] H. Shi, Z. Niu, H. Wang, W. Ye, K. Xi, X. Huang, H. Wang, Y. Liu, H. Lin, H. Shi, Z. An, *Chem. Sci.* **2022**, *13*, 4406–4412.
[29] D. Kim, J. E. Kwon, S. Y. Park, *Adv. Funct. Mater.* **2018**, *28*, 1706213.
[30] J. Ren, Y. Wang, Y. Tian, Z. Liu, X. Xiao, J. Yang, M. Fang, Z. Li, *Angew. Chem. Int. Ed.* **2021**, *60*, 12335–12340.
[31] L. Gu, H. Shi, M. Gu, K. Ling, H. Ma, S. Cai, L. Song, C. Ma, H. Li, G. Xing, X. Hang, J. Li, Y. Gao, W. Yao, Z. Shuai, Z. An, X. Liu, W. Huang, *Angew. Chem. Int. Ed.* **2018**, *57*, 8425–8431.
[32] E. Lucenti, A. Forni, C. Botta, L. Carlucci, A. Colombo, C. Giannini, D. Marinotto, A. Previtali, S. Righetto, E. Cariati, *ChemPhotoChem* **2018**, *2*, 801–805.
[33] C. Giannini, A. Forni, D. Malpicci, E. Lucenti, D. Marinotto, A. Previtali, L. Carlucci, E. Cariati, *Eur. J. Org. Chem.* **2021**, *2021*, 2041–2049.
[34] A. Previtali, E. Lucenti, A. Forni, L. Mauri, C. Botta, C. Giannini, D. Malpicci, D. Marinotto, S. Righetto, E. Cariati, *Molecules* **2019**, *24*, 2552.
[35] E. Lucenti, A. Forni, A. Previtali, D. Marinotto, D. Malpicci, S. Righetto, C. Giannini, T. Virgili, P. Kabacinski, L. Ganzer, U. Giovanella, C. Botta, E. Cariati, *Chem. Sci.* **2020**, *11*, 7599–7608.
[36] A. Previtali, W. He, A. Forni, D. Malpicci, E. Lucenti, D. Marinotto, L. Carlucci, P. Mercandelli, M. A. Ortenzi, G. Terraneo, C. Botta, R. T. K. Kwok, J. W. Y. Lam, B. Z. Tang, E. Cariati, *Chem. Eur. J.* **2021**, *27*, 16690–16700.
[37] D. Malpicci, C. Giannini, E. Lucenti, A. Forni, D. Marinotto, E. Cariati, *Photochemistry* **2021**, *1*, 477–487.
[38] E. Lucenti, A. Forni, C. Botta, C. Giannini, D. Malpicci, D. Marinotto, A. Previtali, S. Righetto, E. Cariati, *Chem. Eur. J.* **2019**, *25*, 2452–2456.
[39] D. Malpicci, A. Forni, C. Botta, C. Giannini, E. Lucenti, D. Marinotto, D. Maver, L. Carlucci, E. Cariati, *Dyes Pigm.* **2023**, *215*, 111274.
[40] P. Data, Y. Takeda, *Chem. Asian J.* **2019**, *14*, 1613–1636.
[41] H. Ma, A. Lv, L. Fu, S. Wang, Z. An, H. Shi, W. Huang, *Ann. Phys.* **2019**, *531*, 1–14.
[42] W. Zhao, Z. He, B. Z. Tang, *Nat. Rev. Mater.* **2020**, *5*, 869–885.
[43] S. Hirata, *J. Phys. Chem. Lett.* **2018**, *9*, 4251–4259.
[44] X.-F. Wang, H. Xiao, P.-Z. Chen, Q.-Z. Yang, B. Chen, C.-H. Tung, Y.-Z. Chen, L.-Z. Wu, *J. Am. Chem. Soc.* **2019**, *141*, 5045–5050.
[45] C. Chen, Z. Chi, K. C. Chong, A. S. Batsanov, Z. Yang, Z. Mao, Z. Yang, B. Liu, *Nat. Mater.* **2021**, *20*, 175–180.
[46] C. Chen, K. C. Chong, Y. Pan, G. Qi, S. Xu, B. Liu, *ACS Materials Lett.* **2021**, *3*, 1081–1087.
[47] S. Yuan, Y. Zhang, J. Chen, Y. Yu, L. Yue, Q. Sun, H. Zhang, S. Xue, W. Yang, *Adv. Opt. Mater.* **2022**, 2200090.
[48] L. Yue, S. Yuan, Y. Zhang, Y. Wang, Q. Sun, H. Zhang, S. Xue, W. Yang, *J. Phys. Chem. Lett.* **2021**, *12*, 11616–11621.
[49] Y. Zhang, Q. Sun, J. Chen, S. Cui, H. Zhang, S. Xue, W. Yang, *Chem. Eng. J.* **2022**, *447*, 137458.
[50] D. Barman, M. Annadhasan, R. Chandrasekar, P. K. Iyer, *Chem. Sci.* **2022**, 9004–9015.
[51] J. Song, Y. Wang, L. Qu, L. Fang, X. Zhou, Z. X. Xu, C. Yang, P. Wu, H. Xiang, *J. Phys. Chem. Lett.* **2022**, *13*, 5838–5844.
[52] J. Yuan, R. Chen, X. Tang, Y. Tao, S. Xu, L. Jin, C. Chen, X. Zhou, C. Zheng, W. Huang, *Chem. Sci.* **2019**, *10*, 5031–5038.
[53] L. Song, X. Wang, M. Zhang, W. Jia, Q. Wang, W. Ye, H. Wang, A. Lv, H. Ma, L. Gu, H. Shi, Z. An, W. Huang, *CCS Chem.* **2021**, *3*, 466–472.
[54] S. Cai, H. Shi, Z. Zhang, X. Wang, H. Ma, N. Gan, Q. Wu, Z. Cheng, K. Ling, M. Gu, C. Ma, L. Gu, Z. An, W. Huang, *Angew. Chem. Int. Ed.* **2018**, *57*, 4005–4009.
[55] K. Suzuki, A. Kobayashi, S. Kaneko, K. Takehira, T. Yoshihara, H. Ishida, Y. Shiina, S. Oishi, S. Tobita, *Phys. Chem. Chem. Phys.* **2009**, *11*, 9850–9860.
[56] G. M. SADABS Sheldrick, *Area Detector Absorption Correction*, University Of Gottingen, Gottingen, Germany, Bruker AXS Inc., Madison, Wisconsin, USA., **2012**.
[57] G. Sheldrick, *Acta Cryst. Sect. A* **2008**, *A64*, 112–122.
[58] G. M. Sheldrick, *Acta Cryst. Sect. C, Struct. Chem.* **2015**, *71*, 3–8.
[59] M. J. Frisch, G. W. Trucks, H. B. Schlegel, G. E. Scuseria, M. A. Robb, J. R. Cheeseman, J. A. Montgomery Jr., T. Vreven, K. N. Kudin, J. C. Burant, et al. *Gaussian 16, Revision A.03; Gaussian, Inc.*, Wallingford, CT, USA, **2016**.
[60] D. Malpicci, E. Lucenti, A. Forni, D. Marinotto, A. Previtali, L. Carlucci, P. Mercandelli, C. Botta, S. Righetto, E. Cariati, *Inorg. Chem. Front.* **2021**, *8*, 1312–1323.
[61] A. Forni, E. Cariati, L. Carlucci, E. Lucenti, D. Marinotto, S. Pieraccini, M. Sironi, *Acta Cryst. Sect. B Struct. Sci. Cryst. Eng. Mater.* **2021**, *77*, 865–870.
[62] J.-D. Chai, M. Head-Gordon, *J. Chem. Phys.* **2008**, *128*, 84106.

Manuscript received: March 23, 2023
Accepted manuscript online: April 21, 2023
Version of record online: May 17, 2023